

KEK Preprint 2000-113  
KUDP 2000-001  
TUAT-HEP 2000-04  
KINDAI-HEP 00-01  
November 2000  
H

## Lorentz Angle Measurement for CO<sub>2</sub>/Isobutane Gas Mixtures

*K.Hoshina<sup>b</sup>, K.Fujii<sup>a</sup>, N.Khalatyan<sup>c</sup>, O.Nitoh<sup>b</sup>, H.Okuno<sup>a</sup>,  
Y.Kato<sup>e</sup>, M.Kobayashi<sup>a</sup>, Y.Kurihara<sup>a</sup>, H.Kuroiwa<sup>b</sup>, Y.Nakamura<sup>b</sup>,  
K.Sakieda<sup>b</sup>, Y.Suzuki<sup>b</sup>, T.Watanabe<sup>d</sup>*

<sup>a</sup> High Energy Accelerator Research Organization(KEK), Tsukuba, 305-0801, Japan

<sup>b</sup>Tokyo University of Agriculture and Technology, Tokyo 184-8588, Japan

<sup>c</sup>Institute of applied physics, University of Tsukuba, 305-8573, Japan

<sup>d</sup>Kogakuin University, Tokyo 163-8677, Japan

<sup>e</sup>Kinki University, Osaka, 577-0085, Japan

### Abstract

We have developed a Lorentz angle measurement system for cool gas mixtures in the course of our R&D for a proposed JLC central drift chamber (JLC-CDC). The measurement system is characterized by the use of two laser beams to produce primary electrons and flash ADCs to read their signals simultaneously. With this new system, we have measured Lorentz angles for CO<sub>2</sub>/isobutane gas mixtures with different proportions (95:5, 90:10, and 85:15), varying drift field from 0.6 to 2.0 kV/cm and magnetic field up to 1.5 T. The results of the measurement are in good agreement with GARFIELD/MAGBOLTZ simulations.

*Keywords:* Lorentz angle; CO<sub>2</sub>/isobutane; Drift chamber; JLC

# 1 Introduction

In order to make maximum use of the full physics potential of a future linear collider such as JLC [1], it is highly desirable that its detector system allows reconstruction of final states in terms of known standard-model partons: charged leptons, quarks, gauge bosons, and neutrinos as missing momenta. Among these partons, lighter quarks ( $u, d, s, c$ , and  $b$ ) and gluons can be detected as jets with or without secondary or tertiary vertices, while heavier partons ( $t, W^\pm$ , and  $Z$ ) can be recognized through calculation of jet invariant masses. The parton reconstruction based on the jet invariant-mass method requires not only efficient and high-resolution tracking of charged particles in a jetty environment, but also good track-cluster matching to achieve the best energy flow measurements. The central tracker should thus be capable of measuring individual charged particles in jets with high efficiency and high momentum resolution, as well as good angular resolution. In order to satisfy these demands, we have proposed, as a candidate JLC central tracker \*, a large cylindrical drift chamber with mini-jet cells filled with a slow gas mixture,  $\text{CO}_2/\text{isobutane}(90:10)$ .

The Lorentz angle, which is the angle between the drift direction of electrons under the influence of magnetic field and the direction of electric field, is one of the key parameters to determine the jet cell design. The existence of the magnetic field tilts drift lines by the Lorentz angle with respect to the electric field direction. If this angle is too big, drift lines for the edge wires hit top or bottom walls of the drift cell, thereby leading us to loss of detection efficiency.

Fig. 1 shows electron drift lines in a jet cell calculated by the chamber simulation program GARFIELD<sup>†</sup> [4] (a) without and (b) with the magnetic field. The results indicate that the drift lines are completely contained in the cell at least up to a magnetic field of 2 T. There is, however, no systematic experimental data published for the Lorentz angles of  $\text{CO}_2/\text{isobutane}$  gas mixtures, which makes difficult for us to test the reliability of our calculations using the GARFIELD program. In order to confirm the results of the GARFIELD calculations and to verify the validity of our cell design, we have developed a Lorentz angle measurement system for cool gas mixtures, which have small Lorentz angles, and carried out systematic measurement for  $\text{CO}_2/\text{isobutane}$  gas mixtures. The measurement system is characterized by the use of two laser beams to produce primary electrons and flash ADCs to read their signals simultaneously.

In this paper we describe the measurement system in detail, present the obtained Lorentz angle data, and compare them with GARFIELD/MAGBOLTZ simulations. The

---

\* Detailed design parameters of the JLC-CDC can be found in our previous papers [2],[3].

<sup>†</sup> GARFIELD provides interfaces to different program packages for calculations of gas properties such as drift velocity, diffusion coefficient, Lorentz angle, etc. Among such interfaces, we used one for MAGBOLTZ, which numerically solves Boltzmann's transport equation for drifting electrons. Unless otherwise specified, the latest version of GARFIELD as of Sep., 2000 (version 7) uses MAGBOLTZ-2[6], which exploits a Monte Carlo integration technique for the solution, whereas the older versions use MAGBOLTZ-1[5] based on an analytic formulation. The two versions yielded consistent results for our gas mixtures at some representative electric and magnetic field values. We thus decided to use the analytic version (version 1.16), since it was impracticable, from computing time point of view, to achieve required accuracy for comparison with all of our data points using the Monte Carlo version (version 2.2) (see Subsection 4.b).

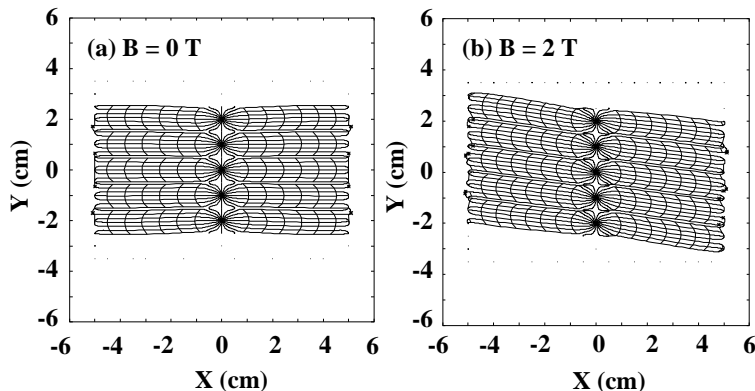


Figure 1: GARFIELD results of electron drift lines and iso-chrones in the JLC-CDC for the CO<sub>2</sub>/isobutane(90:10) gas mixture.

paper is organized as follows: Section 2 introduces some basic formulae relevant to the Lorentz angle measurement, and outlines the design philosophy of our measurement system. Section 3 then describes its hardware aspects, including optical setup, the test chamber geometry, and data acquisition. Section 4 sketches the analysis procedure and presents the Lorentz angle results together with corresponding GARFIELD/MAGBOLTZ predictions. In Section 5, these results are compared with the basic formulae given in Section 2, and their implications are discussed from the view point of application to the JLC-CDC. Finally Section 6 summarizes the results and concludes the paper.

## 2 Principle of Lorentz Angle Measurement

### 2.a A Quick Theoretical Review of the Lorentz Angle

In order to clarify the principal parameters that control the Lorentz angle of drifting electrons, let us start our discussion with deriving a simple expression for the drift velocity vector in the presence of electric and magnetic fields,  $\mathbf{E}$  and  $\mathbf{B}$  [7]. The equation of motion for a drifting electron under the influence of the  $\mathbf{E}$  and  $\mathbf{B}$  fields is given by

$$m \frac{d\mathbf{v}}{dt} = -e (\mathbf{E} + \mathbf{v} \times \mathbf{B}) + m\mathbf{A}(t), \quad (2.1)$$

where  $m$  and  $-e$  are the electron mass and charge, respectively, while  $\mathbf{A}(t)$  is the time-dependent acceleration, or more appropriately deceleration, due to stochastic force (friction) from the surrounding gas molecules. Since we are only interested in a steady state where the electron drifts at a constant drift velocity:  $\mathbf{v}_D \equiv \langle \mathbf{v} \rangle$ , the time-average of the left-hand side of Eq.(2.1) must vanish. The crucial step now is to assume that the time average of  $\mathbf{A}(t)$  is anti-parallel with  $\langle \mathbf{v} \rangle$ :

$$\langle \mathbf{A}(t) \rangle = -\frac{\langle \mathbf{v} \rangle}{\tau}, \quad (2.2)$$

where the constant  $\tau$  has the dimension of time and is called characteristic time which can be related to the average time interval between collisions. The time average of Eq.(2.1)

then becomes

$$0 = -e(\mathbf{E} + \mathbf{v}_D \times \mathbf{B}) - \frac{m}{\tau} \mathbf{v}_D, \quad (2.3)$$

which can be cast into the form:

$$\left( \frac{m}{\tau} - e\mathbf{B} \times \right) \mathbf{v}_D = -e\mathbf{E}. \quad (2.4)$$

Rewriting this as a matrix equation and inverting the matrix, we can solve this for  $\mathbf{v}_D$  and obtain an expression valid for general field configurations:

$$\mathbf{v}_D = \left( \frac{-\mu E}{1 + (\omega\tau)^2} \right) \left( \hat{\mathbf{E}} - (\omega\tau) [\hat{\mathbf{E}} \times \hat{\mathbf{B}}] + (\omega\tau)^2 (\hat{\mathbf{E}} \cdot \hat{\mathbf{B}}) \hat{\mathbf{B}} \right), \quad (2.5)$$

where  $\hat{\mathbf{E}}$  and  $\hat{\mathbf{B}}$  denote unit vectors along  $\mathbf{E}$  and  $\mathbf{B}$ , respectively, while  $\mu$  and  $\omega$  are given by

$$\mu \equiv \left( \frac{e}{m} \right) \tau, \quad \omega \equiv \left( \frac{e}{m} \right) B \quad (2.6)$$

and called mobility and cyclotron frequency, respectively. This solution consists of three components: one parallel with  $\mathbf{E}$ , another parallel with  $\mathbf{B}$ , and the rest orthogonal to both  $\mathbf{E}$  and  $\mathbf{B}$ . When  $\omega\tau \simeq 0$ , which means low magnetic field or short time interval between collisions,  $\mathbf{v}_D$  tends to the  $\mathbf{E}$  field direction. On the other hand, when  $\omega\tau \gg 1$ , the electron curls up into the  $\mathbf{B}$  field direction, as long as  $\mathbf{E} \cdot \mathbf{B} \neq 0$ .

It is easy now to derive from Eq.(2.5) general expressions for the magnitude of  $\mathbf{v}_D$ ,  $v_D = |\mathbf{v}_D|$ :

$$v_D = \mu E \sqrt{\frac{1 + (\hat{\mathbf{E}} \cdot \hat{\mathbf{B}})^2 (\omega\tau)^2}{1 + (\omega\tau)^2}}, \quad (2.7)$$

and the magnitudes of parallel and perpendicular components of  $\mathbf{v}_D$ ,  $v_{D\parallel} = |\mathbf{v}_{D\parallel}|$  and  $v_{D\perp} = |\mathbf{v}_{D\perp}|$ , to the  $\mathbf{E}$  field:

$$v_{D\parallel} = \mu E \frac{1 + (\hat{\mathbf{E}} \cdot \hat{\mathbf{B}})^2 (\omega\tau)^2}{1 + (\omega\tau)^2} \quad (2.8)$$

and

$$v_{D\perp} = \mu E \omega\tau \frac{|\hat{\mathbf{E}} \times \hat{\mathbf{B}}| \sqrt{1 + (\hat{\mathbf{E}} \cdot \hat{\mathbf{B}})^2 (\omega\tau)^2}}{1 + (\omega\tau)^2}. \quad (2.9)$$

Dividing Eq.(2.9) by Eq.(2.8), we thus arrive at the following equation for the Lorentz angle  $\alpha$ :

$$\tan \alpha = \frac{|\hat{\mathbf{E}} \times \hat{\mathbf{B}}|}{\sqrt{1 + (\hat{\mathbf{E}} \cdot \hat{\mathbf{B}})^2 (\omega\tau)^2}} \omega\tau. \quad (2.10)$$

For completeness, we show below the formula for angle  $\beta$  that is the angle between  $\mathbf{v}_{D\perp}$  and  $\hat{\mathbf{E}} \times \hat{\mathbf{B}}$ :

$$\tan \beta = (\hat{\mathbf{E}} \cdot \hat{\mathbf{B}}) \omega \tau. \quad (2.11)$$

If  $\mathbf{E}$  and  $\mathbf{B}$  are mutually orthogonal,  $\hat{\mathbf{E}} \cdot \hat{\mathbf{B}} = 0$ , as in our cell design, we then have  $|\hat{\mathbf{E}} \times \hat{\mathbf{B}}| = 1$ , which leads us to a simple set of equations:

$$v_D = \frac{\mu E}{\sqrt{1 + (\omega \tau)^2}} \quad (2.12)$$

and

$$\tan \alpha = \omega \tau, \quad (2.13)$$

while  $\tan \beta = 0$  meaning that  $\mathbf{v}_{D\perp}$  is perpendicular to both  $\mathbf{E}$  and  $\mathbf{B}$ . It is remarkable that the Lorentz angle is determined by just two parameters  $\omega$  and  $\tau$ , where only  $\tau$  reflects the complexity involved in the electron drift process.

Using Eqs.(2.6) and (2.12) and assuming that  $\tau$  is independent of  $B$ , we can rewrite Eq.(2.13) in the following form:

$$\tan \alpha = \left(\frac{B}{E}\right) v_D^0, \quad (2.14)$$

where  $v_D^0 = v_D(B = 0)$ . On the other hand, the Lorentz angle is often parameterized [8][9] empirically as

$$\tan \alpha = \psi \left(\frac{B}{E}\right) v_D^0, \quad (2.15)$$

where the dimensionless factor  $\psi$  is called a magnetic deflection coefficient. The above formulation thus predicts  $\psi = 1$ . We shall return to this point later in Section 5.

## 2.b Theoretical Expectation for CO<sub>2</sub>/isobutane Gas Mixtures

The formulae presented above allow us to estimate Lorentz angles for CO<sub>2</sub>/isobutane gas mixtures for a given set of  $\mathbf{E}$  and  $\mathbf{B}$  fields. For instance, Eq.(2.14) predicts that the Lorentz angle is proportional to the drift velocity. Because of low drift velocity, any cool gas mixture such as those having CO<sub>2</sub> as their main component must have a small Lorentz angle. For example, our candidate gas mixture for the JLC-CDC, CO<sub>2</sub>/isobutane (90:10), has a drift velocity of  $v_D^0 = 0.78 \text{ cm}/\mu\text{s} = 7.8 \text{ }\mu\text{m}/\text{ns}$  at  $E = 1.0 \text{ kV}/\text{cm} = 100 \text{ kV}/\text{m}$ . At  $B = 1 \text{ T}$  this drift velocity can be translated into a Lorentz angle of

$$\tan \alpha = \left(\frac{B}{E}\right) v_D^0 = \frac{1 \text{ [T]}}{100 \text{ [kV/m]}} \times 7.8 \text{ }[\mu\text{m}/\text{ns}] = 0.078. \quad (2.16)$$

This angle corresponds to a transverse displacement of about 1.5 mm for a drift distance of 2 cm. Since Lorentz angle measurements are mostly based on the determination of this transverse displacement, high resolution and low systematic error are key requirements for its measurement. For instance, an error of 50  $\mu\text{m}$  on the displacement, already amounts to a relative error of about 3 % on  $\tan \alpha$  for the aforementioned sample case.

## 2.c Basic Principle of the Measurement

Basic principle of the Lorentz angle determination is as follows. Consider a cluster of electrons drifting along a uniform electric field ( $\mathbf{E}$ ) applied in the direction of the  $z$ -axis. The presence of a uniform magnetic field ( $\mathbf{B}$ ) in the direction of the  $y$ -axis deflects the drift direction towards the  $x$ -axis. The transverse displacement ( $\Delta x$ ) after drifting over a given distance ( $\Delta z$ ) is a direct measure of the Lorentz angle:

$$\tan \alpha = \frac{\Delta x}{\Delta z}. \quad (2.17)$$

In principle, we thus need to measure just  $\Delta x$  and  $\Delta z$ , provided that  $\mathbf{E}$  and  $\mathbf{B}$  are uniform, orthogonal, stable, and known.

In practice, the uniform electric field is provided by field-shaping plates in a drift chamber. The measurement of the transverse displacement,  $\Delta x$ , can not be made without interfering with the drifting electron cluster: we need to lead the cluster to a gas amplification region, where the  $\mathbf{E}$  field varies quite drastically. The drift region where the  $\mathbf{E}$  field is required to be uniform thus has to be separated from the amplification region with a separating slit. The complexity involved near the slit and in the amplification region has to be somehow canceled. On the other hand, the measurement of  $\Delta z$  seems rather straightforward, since we can control the starting point of the drifting electron cluster, for instance, by controlling the position of the injection point of a laser beam that creates the cluster. It is, however, non-trivial to measure the laser beam position at the ionization point. In the following subsection, we will explain how to avoid these potential problems.

## 2.d Our Measurement System

In order to cancel the effects of the complicated processes due to the non-uniform field near the slit and in the amplification region, it is a common practice[10, 11] to create primary electron clusters at different  $z$  points ( $z_1$  and  $z_2$ ), by moving a laser beam in the  $z$  direction, and measure their arrival points ( $x_1$  and  $x_2$ ) at detecting electrodes. In our case, the electron clusters pass through the slit and then arrive at a sense anode wire strung perpendicular to both  $\mathbf{E}$  and  $\mathbf{B}$ . The avalanche locations along the anode wire, corresponding to  $x_1$  and  $x_2$ , are then determined by the charge centroid method with a set of cathode pads behind it. We can then take the differences  $\Delta x = x_2 - x_1$  and  $\Delta z = z_2 - z_1$  to calculate the Lorentz angle. The method assumes that the two starting positions have the same  $x$  coordinate, or if they are different, they can be calibrated by measuring  $\Delta x$  for no magnetic field.

As shown in Subsection 2.b, however, we expect only small transverse displacements for CO<sub>2</sub>-based gas mixtures. Any small systematic change or instability of the laser beam position is a potential source of significant error. Instead of moving the laser beam, we thus decided to split it into two parallel beams and inject them simultaneously at different  $z$  positions. Since the relative distance of the two laser beams is fixed by the splitter and since the relative distance is the only quantity that actually matters, we can cancel most systematics due to systematic shift or instability of the laser beam positions relative to the chamber.

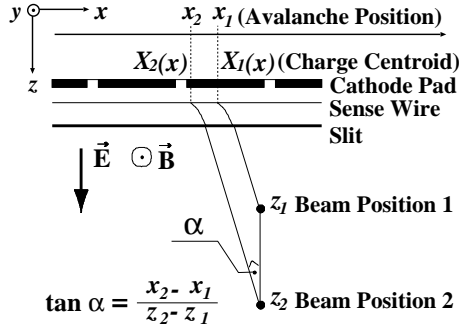


Figure 2: Principle of the Lorentz angle measurement.

Now that two laser beam pulses are injected simultaneously, and since the transverse displacement of the electron clusters is small for our gas mixtures, their induced charge distributions on the cathode pads overlap in space. They are, however, separable in time, since their corresponding drift distances differ. We thus use flash ADCs to record the signal amplitudes as a function of time, and reconstruct individual induced charge distributions on the cathode pads. Fig. 3 illustrates how our DAQ system enables us to separately measure the individual charge centroids of the two electron clusters.

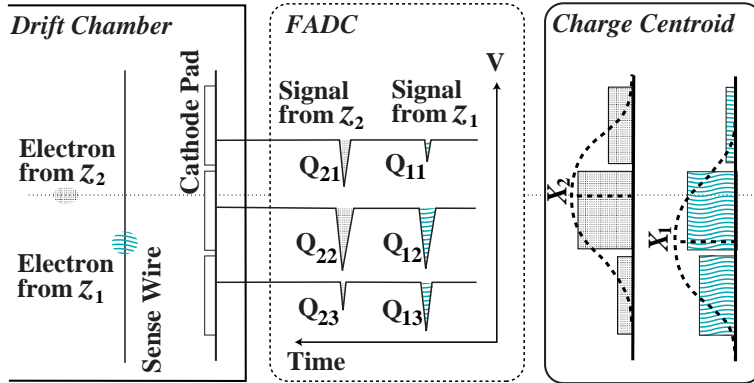


Figure 3: Data acquisition scheme.

The advantages of this two-beam system can be summarized as follows:

- We can eliminate most of the effects of spatial jitters of the laser beams with respect to the chamber. Figure 4 demonstrates how powerful this scheme is in the case of occasional instability we experienced for higher magnetic fields. The oscillations of the two arrival points are coherent and therefore can be canceled by taking their difference.
- We can calibrate the laser beam distance ( $\Delta z = z_2 - z_1$ ) by using the recorded time interval of the two anode pulses, provided that the drift velocity has been measured separately. It should be stressed here that this measures the laser beam distance at the very points of ionization.

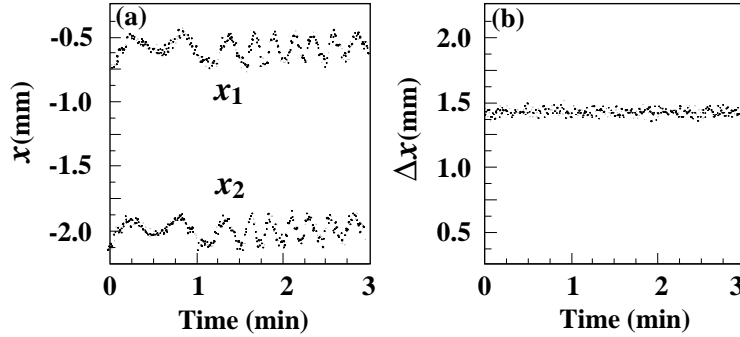


Figure 4: Example of occasional instability observed at  $B = 1.2$  T in the time-dependence of (a) the arrival points of two electron clusters ( $x_1$  and  $x_2$ ). The oscillation is absent from their difference as shown in (b).

- Baselines or pedestals for the cathode pad signals can be monitored on an event-by-event basis.
- The two arrival points are measured with the same set of cathode pads, which is a virtue of slow gas mixtures with small Lorentz angles, thereby reducing systematic errors due to channel-to-channel variation of the readout electronics.

There are, however, some drawbacks: among them potentially the most serious problem, which deserves special attention, is the space-charge effect of the avalanche formed by the first electron cluster on the second one. We will discuss this in Section 4.a.

### 3 Experimental Setup

In this section, we describe how we realized the idea presented above in a real hardware form. Our measurement system can be divided into three major parts: (1) a laser beam system including a laser pulse generator and an optical system to prepare two parallel laser beams, (2) a cathode-readout drift chamber and its gas system, together with a dipole magnet to supply a magnetic field in the chamber's drift region, and (3) a data acquisition system featuring flash ADCs to record the time-profiles of signals from the cathode pads. A schematic view of the setup is shown in Fig. 5, and in what follows, we will describe these three parts in more detail.

#### 3.a Laser Beam System

The laser beam system can be subdivided into a laser pulse generator and an optical system including a beam splitter. An Nd-YAG laser with a wave length of 266 nm generates beam pulses having energies up to 50 mJ and a duration of about 5 nsec at a frequency of 10 Hz. The intensity of the laser beam is reduced to 3 % while reflected by a quartz prism. It is then focused with a lens having a focal length of 3 m, and reflected twice with a pair of 45° mirrors, the second of which is mounted on a micrometer-adjustable mover and allows us to move the laser beam along the  $x$ -axis. The reflected beam is split



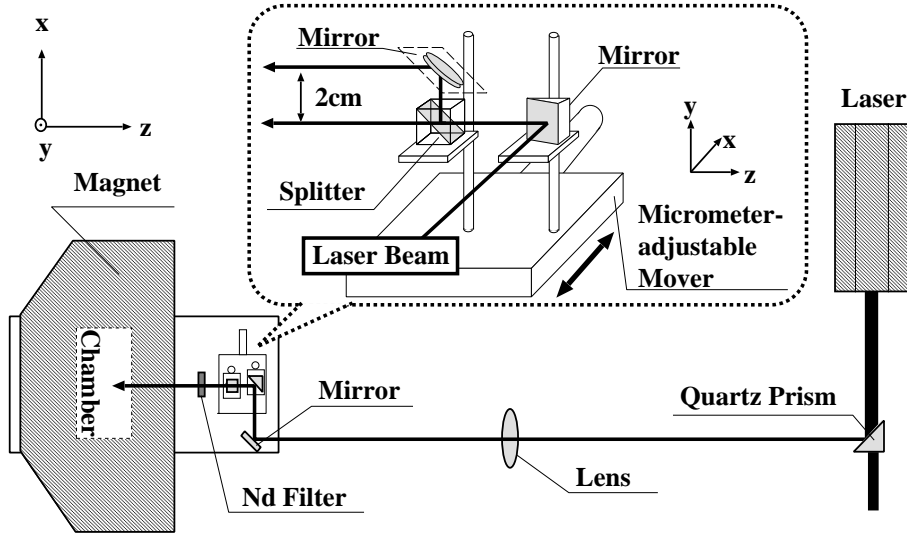


Figure 5: Schematic view of the experimental setup, where our coordinate axes are also defined.

into two beams by a cubic splitter consisting of two prisms glued together[12]: a part of the beam is reflected upward at the boundary, while the rest passes straight through. The upward beam is reflected again by yet another  $45^\circ$  mirror placed 2 cm apart from the splitter, and goes in parallel with the straight-through beam. In order to control the relative intensities of the split beams, we put an ND filter in the way of the pass-through beam. The two laser beams are now ready for disposal at the chamber.

### 3.b Drift Chamber

Our Lorentz angle measurement chamber[13] has a structure depicted in Figs. 6-(a) and (b) and is placed in a uniform magnetic field up to 1.5 T provided by a dipole magnet named USHIWAKA in the KEK-PS  $\pi 2$  beam line. The magnet has an aperture of  $54 \times 64 \text{ cm}^2$  and a pole tip length of 30 cm and is capable of providing a maximum field of 1.6 T with a uniformity much better than 1% over the region occupied by the chamber. As seen in Fig. 6-(a), the two laser beams are reflected vertically down, which is the direction of the magnetic field, by a  $45^\circ$  mirror fixed to the chamber. The beams then pass through a quartz window to enter the drift region of the chamber, which is filled with a  $\text{CO}_2$ /isobutane gas mixture with one of the following three proportions: (85 : 15), (90 : 10), and (95 : 5). The proportions were maintained by mixing high-purity  $\text{CO}_2$  and isobutane gases at the corresponding flow rates using a pair of mass flow controllers. The total flow rate was kept constant at 100 cc/min and the temperature and the pressure were continuously monitored throughout the experiment: the temperature was  $T = 291. \pm 1^\circ\text{K}$  and  $P = 767 \pm 2 \text{ mHg}$ . The two laser beams ionize the chamber gas molecules and produce strings of ionization electrons at two different points in the  $z$ -direction. The spent laser beams leave the chamber through another quartz window and are reflected by another  $45^\circ$  mirror to a beam dump.

The produced electron clusters move in a uniform electric field of 0.6 to 2.0 kV/cm

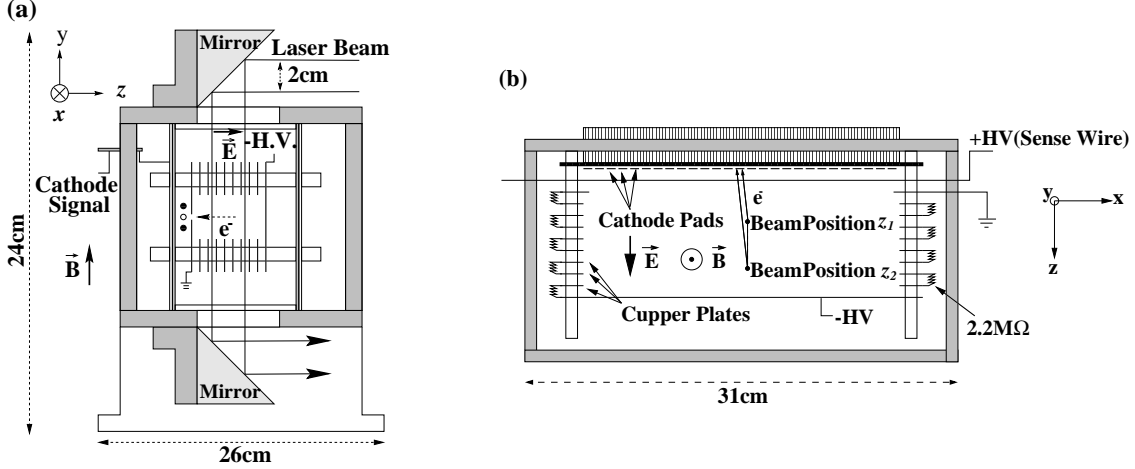


Figure 6: (a) side- and (b) top-views of the drift chamber.

provided by a series of ten 1.0 mm-thick copper plates spaced 5 mm apart and connected with a chain of 2.2 M $\Omega$  resistors (see Fig. 6-(b)). All of these copper plates have an outer size of 30 mm  $\times$  170 mm, among which the middle eight have a rectangular hole of 10 mm  $\times$  130 mm that defines the transverse size of the drift region. The last plate, which is grounded, has a slit of 3 mm  $\times$  130 mm and separates the drift region and the amplification region behind it. In the amplification region, we have a gold-plated tungsten anode wire with a diameter of 30  $\mu$ m strung 5 mm away from and in alignment with the slit. A typical high voltage applied to the anode wire is 2.4 kV. The anode wire is accompanied, in parallel, by a pair of 120  $\mu$ m-thick gold-plated Molybdenum wires strung 5 mm below and above. On the opposite side of the slit, 5 mm apart from the anode wire, there are a series of 27 gold-coated cathode pads each being 4.8 mm in width and 20.0 mm in height. The inter-pad gap is 0.2 mm. In this experiment, however, we used only three of these cathode pads in the central region to measure the charge centroids, due to the smallness of Lorentz angles for our gas mixtures.

### 3.c DAQ System

A block diagram of the data acquisition system is shown in Fig. 7. The signals from the

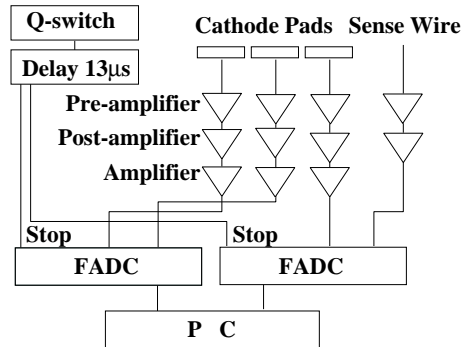


Figure 7: Block diagram for our data acquisition system.

three pads and the anode wire are first amplified by charge-sensitive pre-amplifiers, and, after passing through a 3 m-long twisted pair cable, amplified again by post-amplifiers[14]. The cathode pad signals need further amplification because of their smallness. We thus put an amplifier with a gain of 8 for each of the three pad signals. After these amplifications, the signals are fed into a set of 8-bit flash-ADCs[15] which have a 500 MHz sampling frequency over a 1.6  $\mu$ s time window. The flash ADCs convert the analog amplitudes from 0 V to  $-1.0$  V into a train of digits ranging from 255 to 0 every 2 ns. Finally, these flash ADC outputs are recorded by a PC through a CAMAC system.

## 4 Analysis and Results

### 4.a Analysis

As we discussed in Subsection 2.c, Lorentz angle is obtained by measuring the transverse distance  $\Delta x$  between the arrival points at the anode wire of two electron clusters created in the drift region at a distance  $\Delta z$  in the electric field direction. By means of the cathode pads and flash ADCs connected to them, avalanche locations that correspond to the arrival points of the two electron clusters ( $x_1$  and  $x_2$ ) are encoded as induced-charge distributions. The  $\Delta z$ , corresponding to the beam distance in the electric field direction, is determined by the optical system and can be calculated from the time interval ( $\Delta t$ ) of the two pulses at  $B = 0$ , together with a pre-measured drift velocity ( $v_D^0$ ) as  $\Delta z = v_D^0 \cdot \Delta t$ .

Decoding of the  $\Delta x$  information, on the other hand, requires a mapping from the charges on the three cathode pads to a position in the anode wire direction (the  $x$ -axis). It is a common practice to use, as a measure of this position, the charge centroid as defined by

$$X = \frac{\sum_{i=1}^3 x^i Q_i}{\sum_{i=1}^3 Q_i} \quad (4.1)$$

where  $x^i$  and  $Q_i$  are the central position and the collected charge of the  $i$ -th cathode pad, respectively. The charge centroid ( $X$ ) as defined above, however, doesn't reproduce the actual avalanche position ( $x$ ) of an electron cluster, because of the finite width and number of the cathode pads used in the calculation. This necessitates a calibration curve to map  $X$  to  $x$ . This map has been obtained by scanning the laser beam along the  $x$ -axis with a step of 200  $\mu$ m by moving the micrometer-adjustable mirror described in Subsection 3.a (see Figs. 5 and 8). Figure 9 is an example of so obtained calibration curves.

Another way to map the charge information to the position is to use the relation between the position and the ratio of the charge on a side pad to that on the central pad. There are two ratios available,  $R_L \equiv Q_1/Q_2$  and  $R_R \equiv Q_3/Q_2$ . Their sensitivity to the position varies: the sensitivity of  $R_{L(R)}$  attains its maximum near the boundary of the left(right) and central pads and monotonically diminishes towards the other pad boundary. This is demonstrated in Fig. 10 which is an example of the ratio-position relations obtained from the calibration data we took for the charge centroid method.

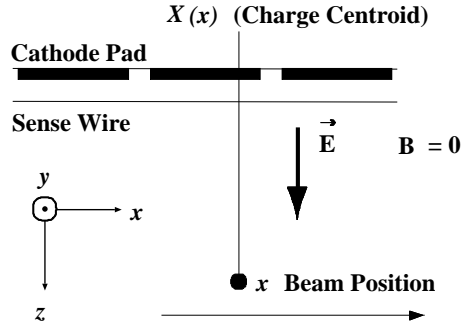


Figure 8: Calibration scheme. Cathode signals are recorded with the same readout electronics as used in the actual Lorentz angle measurement together with the actual laser beam position ( $x$ ) as obtained from micrometer readings.

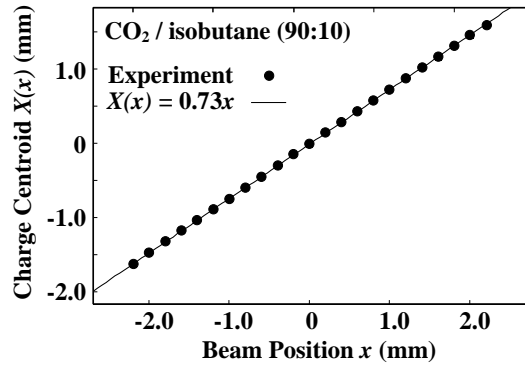


Figure 9: Charge centroid ( $X$ ) as defined in the text as a function of the injection point ( $x$ ) of the laser beam, which is used as a calibration curve.

Since the two ratios are complementary, we can combine their information:

$$x = \frac{\frac{1}{\sigma_{x(R_L)}^2} \cdot x(R_L) + \frac{1}{\sigma_{x(R_R)}^2} \cdot x(R_R)}{\frac{1}{\sigma_{x(R_L)}^2} + \frac{1}{\sigma_{x(R_R)}^2}}. \quad (4.2)$$

Hereafter, we call this method the ratio method. The ratio method allows us to bypass the calculation of an intermediate quantity,  $X$ , and is expected to work better near the pad boundaries. The charge centroid method, on the other hand, performs better near the center of the central pad. In this sense, the two methods are complementary.

In either case, the central issue is what determines the calibration curves. For simplicity, let us consider first the case of a single beam. The induced-charge distribution of the cathode pads is determined not only by the location, but also by the shape (charge distribution) of the avalanche. The avalanche shape is affected by the shape of the electron cluster that initiates the avalanche, which in turn depends on the diffusion that varies with the gas mixture and the electric field. The avalanche shape is also controlled by the field around the anode wire and the gas mixture, in particular when the gas amplification process approaches streamer mode operation. In order to check the potential dependence

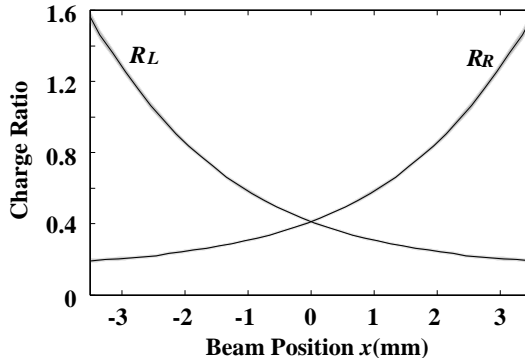


Figure 10: Left and right charge ratios as defined in the text as a function of the injection point ( $x$ ) of the laser beam, which is used as a calibration curve. The shaded bands indicate 1- $\sigma$  error boundaries.

on these parameters, we took calibration data for various electric fields and for different gas mixtures, at several sense-wire high-voltages. There is no significant correlation seen between these parameters and the calibration curves, which led us to conclude that the charge centroid ( $X$ ) is a function of a single quantity: the avalanche location ( $x$ ) in the single beam case.

The determination of  $\Delta x$ , however, requires double beams. We thus have to discuss now the space charge effect of the avalanche created by the first electron cluster on the second one. There are two possible ways for the first avalanche to affect the second: (1) the first avalanche changes the shape of the second through space charge effects, and (2) the first avalanche bends the trajectory of the second electron cluster near the sense wire. Possibility (1) was eliminated by comparing the calibration curves of the two pulses: there was no difference. In order to test possibility (2), we changed the intensity of the laser beam to create the first electron cluster and monitored  $\Delta x$  with no magnetic field, varying the electric field to change the time interval of the two avalanche formations. We saw no significant dependence of  $\Delta x$  on the beam intensity nor the electric field  $\mathbf{E}$ . We thus confirmed that space charge effect is negligible in our measurement range.

## 4.b Results

Using the  $\Delta z$  and the  $\Delta x$  values obtained with the calibration curve discussed above, we calculated the Lorentz angles for different CO<sub>2</sub>/isobutane gas mixtures. The results are shown in Figs. 11-(a), -(b), and -(c) as a function of the electric field for three mixing ratios: (85 : 15), (90 : 10), and (95 : 5). At each electric field value in each figure, seven points are plotted, corresponding to, from bottom to top, seven magnetic field values: 0.0, 0.3, 0.5, 0.75, 1.0, 1.2, and 1.5 T, respectively\*. Their numerical values are tabulated in Table.1.

The errors contain both statistical and systematic ones. The statistical errors have

---

\* Knowing that the Lorentz angle and consequently the transverse displacement  $\Delta x$  have to vanish at  $B = 0$ , we averaged the zero magnetic field data for each gas mixture to determine the offset due to the transverse misalignment of the two laser beams.

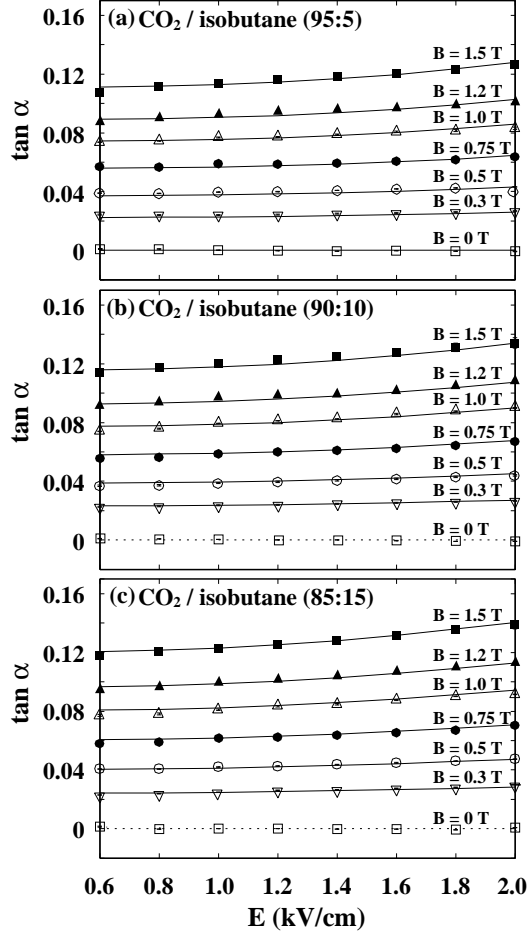


Figure 11: Tangent of the Lorentz angle ( $\tan \alpha$ ) as a function of the electric field for  $\text{CO}_2$ /isobutane mixtures of (a) (95:5), (b) (90:10), and (c) (85:15). Smooth curves are GARFIELD/MAGBOLTZ predictions.

been calculated from the number of events and found negligible for most cases, since a typical resolution for the transverse distance ( $\Delta x$ ) was as small as  $\sigma_{\Delta x} = 40 \mu\text{m}$ . On the other hand, possible sources of systematic errors include

- temperature and pressure dependence: negligible,
- laser beam distance: less than  $250 \mu\text{m}$  by a direct survey and was confirmed by the measured time interval of the two anode pulses at  $B = 0$ ,
- misalignment of the optical system with respect to the chamber: negligible as long as  $\Delta z$  is measured at the points of ionization,
- the electric field value: checked with GARFIELD and the field uniformity was confirmed to be much better than 1 %,
- non-uniformity of the magnetic field : well below 1 %,
- the charge-to-position conversion methods: dominant.

CO <sub>2</sub> /isobutane (85:15)		CO <sub>2</sub> /isobutane (90:10)		CO <sub>2</sub> /isobutane (95:05)	
E(kV/cm)	tan $\alpha$	E(kV/cm)	tan $\alpha$	E(kV/cm)	tan $\alpha$
B = 0.3 T					
0.6	$(2.29 \pm 0.02) \times 10^{-2}$	0.6	$(2.25 \pm 0.04) \times 10^{-2}$	0.6	$(2.43 \pm 0.04) \times 10^{-2}$
0.8	$(2.39 \pm 0.03) \times 10^{-2}$	0.8	$(2.30 \pm 0.04) \times 10^{-2}$	0.8	$(2.38 \pm 0.04) \times 10^{-2}$
1.0	$(2.48 \pm 0.03) \times 10^{-2}$	1.0	$(2.35 \pm 0.04) \times 10^{-2}$	1.0	$(2.39 \pm 0.04) \times 10^{-2}$
1.2	$(2.61 \pm 0.03) \times 10^{-2}$	1.2	$(2.39 \pm 0.04) \times 10^{-2}$	1.2	$(2.44 \pm 0.04) \times 10^{-2}$
1.4	$(2.65 \pm 0.03) \times 10^{-2}$	1.4	$(2.47 \pm 0.04) \times 10^{-2}$	1.4	$(2.49 \pm 0.04) \times 10^{-2}$
1.6	$(2.73 \pm 0.03) \times 10^{-2}$	1.6	$(2.53 \pm 0.04) \times 10^{-2}$	1.6	$(2.54 \pm 0.04) \times 10^{-2}$
1.8	$(2.82 \pm 0.03) \times 10^{-2}$	1.8	$(2.58 \pm 0.04) \times 10^{-2}$	1.8	$(2.60 \pm 0.04) \times 10^{-2}$
2.0	$(2.96 \pm 0.03) \times 10^{-2}$	2.0	$(2.67 \pm 0.04) \times 10^{-2}$	2.0	$(2.66 \pm 0.04) \times 10^{-2}$
B = 0.5 T					
0.6	$(4.05 \pm 0.04) \times 10^{-2}$	0.6	$(3.69 \pm 0.06) \times 10^{-2}$	0.6	$(3.89 \pm 0.04) \times 10^{-2}$
0.8	$(4.07 \pm 0.04) \times 10^{-2}$	0.8	$(3.74 \pm 0.06) \times 10^{-2}$	0.8	$(3.89 \pm 0.04) \times 10^{-2}$
1.0	$(4.20 \pm 0.05) \times 10^{-2}$	1.0	$(3.88 \pm 0.06) \times 10^{-2}$	1.0	$(3.97 \pm 0.04) \times 10^{-2}$
1.2	$(4.27 \pm 0.05) \times 10^{-2}$	1.2	$(3.97 \pm 0.06) \times 10^{-2}$	1.2	$(3.99 \pm 0.04) \times 10^{-2}$
1.4	$(4.36 \pm 0.05) \times 10^{-2}$	1.4	$(4.07 \pm 0.06) \times 10^{-2}$	1.4	$(4.08 \pm 0.04) \times 10^{-2}$
1.6	$(4.49 \pm 0.05) \times 10^{-2}$	1.6	$(4.18 \pm 0.06) \times 10^{-2}$	1.6	$(4.17 \pm 0.04) \times 10^{-2}$
1.8	$(4.61 \pm 0.05) \times 10^{-2}$	1.8	$(4.29 \pm 0.06) \times 10^{-2}$	1.8	$(4.26 \pm 0.04) \times 10^{-2}$
2.0	$(4.75 \pm 0.05) \times 10^{-2}$	2.0	$(4.41 \pm 0.06) \times 10^{-2}$	2.0	$(4.31 \pm 0.04) \times 10^{-2}$
B = 0.75 T					
0.6	$(5.80 \pm 0.06) \times 10^{-2}$	0.6	$(5.56 \pm 0.06) \times 10^{-2}$	0.6	$(5.73 \pm 0.06) \times 10^{-2}$
0.8	$(5.90 \pm 0.06) \times 10^{-2}$	0.8	$(5.67 \pm 0.06) \times 10^{-2}$	0.8	$(5.69 \pm 0.06) \times 10^{-2}$
1.0	$(6.14 \pm 0.06) \times 10^{-2}$	1.0	$(5.87 \pm 0.06) \times 10^{-2}$	1.0	$(5.90 \pm 0.06) \times 10^{-2}$
1.2	$(6.23 \pm 0.06) \times 10^{-2}$	1.2	$(6.01 \pm 0.06) \times 10^{-2}$	1.2	$(5.87 \pm 0.06) \times 10^{-2}$
1.4	$(6.36 \pm 0.06) \times 10^{-2}$	1.4	$(6.10 \pm 0.07) \times 10^{-2}$	1.4	$(5.96 \pm 0.06) \times 10^{-2}$
1.6	$(6.53 \pm 0.07) \times 10^{-2}$	1.6	$(6.24 \pm 0.07) \times 10^{-2}$	1.6	$(6.04 \pm 0.06) \times 10^{-2}$
1.8	$(6.72 \pm 0.07) \times 10^{-2}$	1.8	$(6.45 \pm 0.07) \times 10^{-2}$	1.8	$(6.19 \pm 0.07) \times 10^{-2}$
2.0	$(7.04 \pm 0.07) \times 10^{-2}$	2.0	$(6.71 \pm 0.08) \times 10^{-2}$	2.0	$(6.38 \pm 0.07) \times 10^{-2}$
B = 1.0 T					
0.6	$(7.72 \pm 0.09) \times 10^{-2}$	0.6	$(7.40 \pm 0.08) \times 10^{-2}$	0.6	$(7.36 \pm 0.08) \times 10^{-2}$
0.8	$(7.81 \pm 0.10) \times 10^{-2}$	0.8	$(7.58 \pm 0.08) \times 10^{-2}$	0.8	$(7.45 \pm 0.08) \times 10^{-2}$
1.0	$(8.10 \pm 0.10) \times 10^{-2}$	1.0	$(7.94 \pm 0.08) \times 10^{-2}$	1.0	$(7.67 \pm 0.08) \times 10^{-2}$
1.2	$(8.34 \pm 0.10) \times 10^{-2}$	1.2	$(8.11 \pm 0.08) \times 10^{-2}$	1.2	$(7.73 \pm 0.08) \times 10^{-2}$
1.4	$(8.49 \pm 0.10) \times 10^{-2}$	1.4	$(8.25 \pm 0.08) \times 10^{-2}$	1.4	$(7.88 \pm 0.09) \times 10^{-2}$
1.6	$(8.75 \pm 0.09) \times 10^{-2}$	1.6	$(8.57 \pm 0.10) \times 10^{-2}$	1.6	$(8.07 \pm 0.09) \times 10^{-2}$
1.8	$(9.02 \pm 0.09) \times 10^{-2}$	1.8	$(8.77 \pm 0.10) \times 10^{-2}$	1.8	$(8.14 \pm 0.11) \times 10^{-2}$
2.0	$(9.15 \pm 0.09) \times 10^{-2}$	2.0	$(8.99 \pm 0.10) \times 10^{-2}$	2.0	$(8.30 \pm 0.11) \times 10^{-2}$
B = 1.2 T					
0.6	$(9.41 \pm 0.09) \times 10^{-2}$	0.6	$(9.18 \pm 0.10) \times 10^{-2}$	0.6	$(8.76 \pm 0.09) \times 10^{-2}$
0.8	$(9.65 \pm 0.10) \times 10^{-2}$	0.8	$(9.38 \pm 0.10) \times 10^{-2}$	0.8	$(9.04 \pm 0.09) \times 10^{-2}$
1.0	$(9.95 \pm 0.10) \times 10^{-2}$	1.0	$(9.70 \pm 0.10) \times 10^{-2}$	1.0	$(9.28 \pm 0.09) \times 10^{-2}$
1.2	$(1.01 \pm 0.01) \times 10^{-1}$	1.2	$(9.85 \pm 0.10) \times 10^{-2}$	1.2	$(9.45 \pm 0.09) \times 10^{-2}$
1.4	$(1.04 \pm 0.01) \times 10^{-1}$	1.4	$(9.91 \pm 0.11) \times 10^{-2}$	1.4	$(9.61 \pm 0.10) \times 10^{-2}$
1.6	$(1.07 \pm 0.01) \times 10^{-1}$	1.6	$(1.02 \pm 0.01) \times 10^{-1}$	1.6	$(9.71 \pm 0.10) \times 10^{-2}$
1.8	$(1.10 \pm 0.01) \times 10^{-1}$	1.8	$(1.05 \pm 0.01) \times 10^{-1}$	1.8	$(9.91 \pm 0.10) \times 10^{-2}$
2.0	$(1.13 \pm 0.01) \times 10^{-1}$	2.0	$(1.08 \pm 0.01) \times 10^{-1}$	2.0	$(1.01 \pm 0.01) \times 10^{-1}$
B = 1.5 T					
0.6	$(1.18 \pm 0.02) \times 10^{-1}$	0.6	$(1.14 \pm 0.02) \times 10^{-1}$	0.6	$(1.08 \pm 0.01) \times 10^{-1}$
0.8	$(1.20 \pm 0.01) \times 10^{-1}$	0.8	$(1.17 \pm 0.02) \times 10^{-1}$	0.8	$(1.12 \pm 0.01) \times 10^{-1}$
1.0	$(1.22 \pm 0.02) \times 10^{-1}$	1.0	$(1.20 \pm 0.02) \times 10^{-1}$	1.0	$(1.14 \pm 0.01) \times 10^{-1}$
1.2	$(1.25 \pm 0.02) \times 10^{-1}$	1.2	$(1.23 \pm 0.02) \times 10^{-1}$	1.2	$(1.17 \pm 0.01) \times 10^{-1}$
1.4	$(1.28 \pm 0.02) \times 10^{-1}$	1.4	$(1.25 \pm 0.02) \times 10^{-1}$	1.4	$(1.19 \pm 0.01) \times 10^{-1}$
1.6	$(1.32 \pm 0.02) \times 10^{-1}$	1.6	$(1.28 \pm 0.03) \times 10^{-1}$	1.6	$(1.21 \pm 0.01) \times 10^{-1}$
1.8	$(1.35 \pm 0.02) \times 10^{-1}$	1.8	$(1.31 \pm 0.03) \times 10^{-1}$	1.8	$(1.23 \pm 0.01) \times 10^{-1}$
2.0	$(1.39 \pm 0.03) \times 10^{-1}$	2.0	$(1.34 \pm 0.04) \times 10^{-1}$	2.0	$(1.26 \pm 0.02) \times 10^{-1}$

Table 1: tan  $\alpha$  data

As we discussed at the beginning of this section, there are two methods to convert cathode pad charge information to position information: the charge centroid method and the ratio method. The sensitivity of the two methods differ depending on the location of the center of the induced charge. In general the ratio method works better when the charge center is near the pad boundaries, while the charge centroid method is expected to perform better near the center of the central pad. Because of this, we tried both methods to calculate  $\Delta x$ . In some cases, we found some discrepancies between them. Since there was no a priori reason to prefer particular one to the other, we decided to take the average of the two and put the half of the discrepancy as a systematic error on each point.

Curves in Figs. 11-(a), -(b), and -(c) are predictions obtained with MAGBOLTZ-1 (version 1.16) through its GARFIELD interface, although its accuracy for the velocity distribution of electrons is known to be limited under certain circumstances[16]. The loss of accuracy is caused by a decomposition of the velocity distribution function in Legendre polynomials, in which the lowest two or three terms are retained in the calculation. Therefore results given by the program may not be precise enough when the velocity distribution deviates far from isotropy or it has no axial symmetry as in the case of crossed electric and magnetic fields. On the other hand, our experimental condition seems to be favorable for application of MAGBOLTZ-1: electrons in CO<sub>2</sub>-based gas mixtures under a low electric field are nearly thermal and the axial symmetry of the velocity distribution holds to a good extent, because their Lorentz angles are small even in a high magnetic field. To confirm this we ran the Monte Carlo version (MAGBOLTZ-2, version 2.2[6]), which is free from the problems stated above though time-consuming, to simulate Lorentz angles for several electric and magnetic field combinations. The results were found to be consistent with those obtained with MAGBOLTZ-1.

Our results are in good agreement with the MAGBOLTZ-1 predictions.

## 5 Discussion

### 5.a Magnetic Deflection Coefficient $\psi$

We calculated the magnetic deflection coefficient ( $\psi$ ) from the measured Lorentz angles and the drift velocities obtained without magnetic field. Fig. 12 shows the resultant  $\psi$  as a function of electric field strength for the CO<sub>2</sub>/isobutane(90:10) mixture at  $B = 1.5$  T, while Fig. 13 shows the drift velocity in the absence of magnetic field( $v_D^0$ ). The drift velocity is also listed in Table 2. The values of  $\psi$  were found to be close to unity within  $\pm 5\%$  for the whole range of the applied electric and magnetic fields and for all the gas mixtures used. The gas dependence of the Lorentz angle is shown in Fig. 14. The observed increase of the Lorentz angle with isobutane concentration is consistent with the increase of drift velocity and with  $\psi = 1$ . Why are the values of  $\psi$  so close to unity?

As discussed in Subsection 2.a,  $\psi = 1$  is a straightforward consequence of a simplified model of the force acting on a drifting electron. The model is based on naive expectation for the average force from gas molecules to be anti-parallel with the drift velocity (Eq. 2.2) and a crude assumption that the average time interval between collisions ( $\tau$ ) is not affected by the presence of a magnetic field.



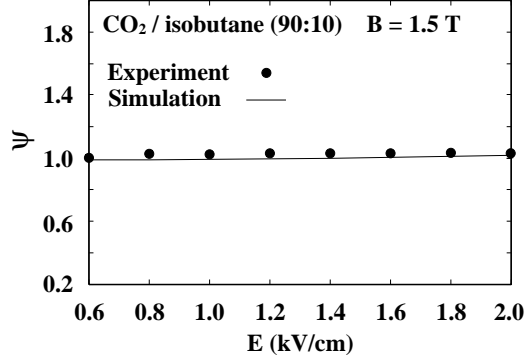


Figure 12: Magnetic deflection coefficient at  $B = 1.5\text{T}$  as a function of the electric field for the  $\text{CO}_2/\text{isobutane}(90:10)$  mixture.

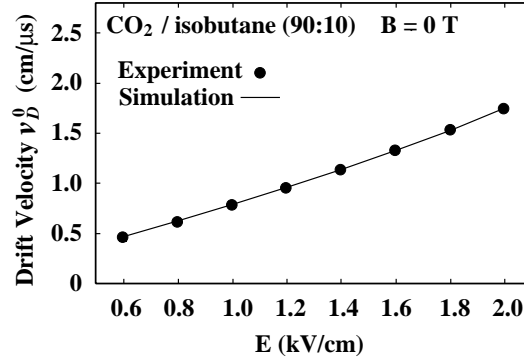


Figure 13: Drift velocity at  $B = 0$  as a function of the electric field for the  $\text{CO}_2/\text{isobutane}(90:10)$  mixture.

In general, however, the average stochastic force, namely the average momentum transfer per unit time from the gas molecules to an electron, is given by

$$\begin{aligned}
 \langle \mathbf{F}_{\text{coll}} \rangle &\equiv m \langle \mathbf{A}(t) \rangle = - \int \nu_m(v) m \mathbf{v} f(\mathbf{v}) d\mathbf{v} \\
 &\simeq -m\nu_m(v_0) \int \mathbf{v} f(\mathbf{v}) d\mathbf{v} - m \left. \frac{d\nu_m}{dv} \right|_{v=v_0} \int (v - v_0) \mathbf{v} f(\mathbf{v}) d\mathbf{v}, \quad (5.1)
 \end{aligned}$$

where  $\nu_m$  is momentum-transfer collision frequency\*,  $f(\mathbf{v})$  represents the normalized random velocity distribution of electrons, and  $v_0$  is an appropriate average value of  $|\mathbf{v}|$ . Thus  $\langle \mathbf{F}_{\text{coll}} \rangle$  is not necessarily anti-parallel with the drift velocity ( $\mathbf{v}_D = \int \mathbf{v} f(\mathbf{v}) d\mathbf{v}$ ) unless  $f(\mathbf{v})$  has axial symmetry with respect to the drift direction (as in the case of no magnetic

\* The momentum transfer collision frequency is given by

$$\begin{aligned}
 \nu_m(|\mathbf{v}|) &\equiv N|\mathbf{v}| \int (1 - \cos \theta) d\sigma \\
 &= N|\mathbf{v}| \sigma (1 - \overline{\cos \theta}),
 \end{aligned}$$

where  $N$  is the density of gas molecules,  $d\sigma$  is the differential cross section, and  $\theta$  is the scattering angle measured from  $\mathbf{v}$ .

E (kV/cm)	$v_D^0$ (cm/ $\mu$ s)
0.6	$0.453 \pm 0.002$
0.8	$0.607 \pm 0.001$
1.0	$0.780 \pm 0.001$
1.2	$0.950 \pm 0.001$
1.4	$1.132 \pm 0.001$
1.6	$1.323 \pm 0.001$
1.8	$1.524 \pm 0.004$
2.0	$1.735 \pm 0.004$

Table 2: Drift velocity data for CO<sub>2</sub>/isobutane (90:10) at  $B = 0$  T.

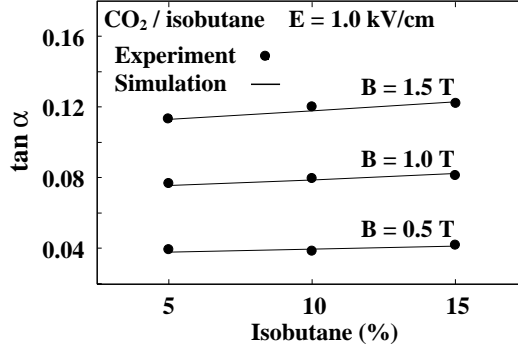


Figure 14: Isobutane concentration dependence of  $\tan \alpha$  at  $E = 1.0$  kV/cm. The solid lines are GARFIELD/MAGBOLTZ predictions.

field) or  $\nu_m$  is independent of  $|\mathbf{v}|$ <sup>†</sup>. Furthermore  $\tau$  ( $\simeq 1/\nu_m(v_0)$ ) does depend on  $B$  since the magnetic field modifies the energy distribution of electrons. Therefore  $\psi$  is not in general expected to be unity.

It may be possible to make the simplified model a little bit more realistic by adding the component of  $\langle \mathbf{F}_{\text{coll}} \rangle$  perpendicular to  $\mathbf{v}_D$  ( $\langle \mathbf{F}_{\text{coll}} \rangle_{\perp}$ ) to the fundamental equation (2.3) and by assuming  $\tau$  to be a function of  $E/N$  and  $B/N$ , where  $N$  is the density of gas molecules.  $\langle \mathbf{F}_{\text{coll}} \rangle_{\perp}$  may be expressed as  $-e K \mathbf{v}_D \times \mathbf{B}$  with  $K$ , again a function of both  $E/N$  and  $B/N$ . The relation (2.14) is then corrected to be

$$\begin{aligned} \tan \alpha &= (1 + K) \frac{eB}{m} \tau \\ &= (1 + K) \left( \frac{\tau}{\tau_0} \right) \left( \frac{B}{E} \right) v_D^0, \end{aligned} \quad (5.2)$$

where  $\tau = \tau(E/N, B/N)$  and  $\tau_0 = \tau(E/N, 0)$ . Therefore the magnetic deflection coefficient is defined by

$$\psi = (1 + K) \frac{\tau}{\tau_0}. \quad (5.3)$$

The sign of  $K$  is positive in most cases. Therefore  $\langle \mathbf{F}_{\text{coll}} \rangle_{\perp}$  shows up as an increase of the apparent strength of  $\mathbf{B}$  in Eq.(2.3) and consequently contributes to make  $\psi$  greater than

<sup>†</sup>In fact the axial symmetry of  $f(\mathbf{v})$  is retained even under a magnetic field when  $\nu_m$  is constant[8].

unity. It is worth mentioning that even in the case where  $B$  is small enough to assure that  $\tau/\tau_0 = 1$ ,  $\psi$  can be greater than unity because of the existence of positive  $K$ <sup>‡</sup>.

In the gas mixtures tested and under the applied electric field ( $\leq 2$  kV/cm), electrons are nearly thermal, i.e., the velocity distribution is close to Maxwellian, and  $\nu_m$  is fairly constant over the main portion of the electron velocity (energy) distribution[19]. Under these conditions, the use of the second line of Eq.(5.1) leads to an approximate expression for the function  $K$ :

$$K \sim \cos^2 \alpha \left( \frac{\nu'_m(v_0)}{\nu_m(v_0)} \right)^2 \langle (\Delta v)^2 \rangle \quad (5.4)$$

with  $\langle (\Delta v)^2 \rangle \equiv \int (v - v_0)^2 f_0(v) dv$ , where  $\nu'_m(v_0) \equiv \left. \frac{d\nu_m}{dv} \right|_{v=v_0}$  and  $f_0(v) \equiv \int v^2 f(\mathbf{v}) d\Omega$ .  $K$  is certainly positive and estimated to be much smaller than one because of small  $\nu'_m(v_0)$ , large  $\nu_m(v_0)$  and the narrow energy distribution. Besides, the variation of  $\tau$  and  $\langle (\Delta v)^2 \rangle$  caused by the magnetic field is insignificant since the energy distribution of electrons is modified little. These facts explain why  $\psi$  is always close to unity in our measurements.

It should be noted that the above argument is justified for relatively low  $E/N$  and  $\psi$  may deviate from unity under higher electric fields as in the case of argon-based gas mixtures [17][18].

## 5.b Extrapolation to 2 T

The current design of the JLC-CDC assumes operation under a magnetic field of 2.0 T. Figure 15 plots the Lorentz angle as a function of the magnetic field. As is expected from Eq.(2.15), the Lorentz angle is proportional to the magnetic field as long as  $\psi = 1$ . We thus fit a straight line passing through the origin to the data points below 1.5 T and extrapolate the line to 2.0 T, in order to estimate the Lorentz angle for the JLC-CDC. At  $E = 1$  kV/cm and  $B = 2$  T the extrapolated Lorentz angle is  $\tan \alpha = 0.159 \pm 0.002$  for the CO<sub>2</sub>/isobutane(90:10) mixture. The shaded band above 1.5 T indicates 1- $\sigma$  extrapolation error interval. The dotted line in the figure is the prediction of GARFIELD/MAGBOLTZ which is consistent with the extrapolation. The JLC cell design shown in Fig. 1 is thus justified.

## 5.c Possibility of Higher Magnetic Field

Motivated mainly by recent studies of beam-induced background[20], possibility of higher magnetic field is now under serious considerations. Our current cell design allows a magnetic field up to about 3 T. Since GARFIELD/MAGBOLTZ reproduces our Lorentz angle data very well, it is plausible that it continues to work well at around 3 T, too. It is, however, desirable to confirm this experimentally. We are thus planning to measure Lorentz angles at higher magnetic fields.

---

<sup>‡</sup> The  $B/N$ -dependence of the function  $K$  and  $\tau$ , and therefore  $\psi$  is expected to be virtually diminished if the effective reduction of  $E/N$  is taken into account[17].

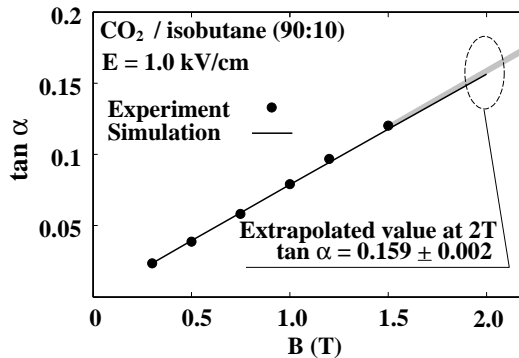


Figure 15:  $\tan\alpha$  at  $E = 1.0$  kV/cm plotted against the magnetic field for the  $\text{CO}_2/\text{isobutane}(90:10)$  mixture. The shaded band above  $B = 1.5$  T is the  $1\text{-}\sigma$  bound for the straight-line extrapolation, while the solid line is the GARFIELD/MAGBOLTZ simulation.

## 6 Conclusions

We have developed a new Lorentz angle measurement system for cool gas mixtures. The measurement system features a laser beam system providing two simultaneous beams to produce primary electrons and a drift chamber with flash ADCs to read their signals. The use of the two simultaneous laser beams and the flash ADCs significantly reduced systematic errors and allowed measurements of small Lorentz angles expected for cool gas mixtures such as  $\text{CO}_2$ -based mixtures.

Using this new system, we have measured Lorentz angles for  $\text{CO}_2/\text{isobutane}$  gas mixtures with different proportions: (95:5, 90:10, and 85:15), varying drift field from 0.6 to 2.0 kV/cm and magnetic field up to 1.5 T. The results of the measurement are in good agreement with GARFIELD/MAGBOLTZ simulations. Our data confirmed the validity of the assumption of the magnetic deflection coefficient being unity in our measurement range. The mixing ratio dependence of the Lorentz angle can thus be understood simply by that of the drift velocity.

We used our data to estimate the Lorentz angle for the current JLC-CDC cell design. At  $E = 1$  kV/cm and  $B = 2$  T the extrapolated Lorentz angle is  $\tan\alpha = 0.159 \pm 0.002$  for the  $\text{CO}_2/\text{isobutane}(90:10)$  mixture, confirming the validity of the current design.

## Acknowledgments

The authors would like to thank all the members of the JLC physics working group. In particular, they are very grateful to Y. Asano, T. Matsui, and S. Iwata for continuous encouragements and supports. This work was supported in part by the JSPS Japanese-German Cooperation Program.

## References

- [1] JLC group, KEK Report 92-16, December (1992).

- [2] Y. Kurihara *et al.*, Nucl. Instr. and Meth. **A441** (2000) 393.
- [3] N. Khalatyan *et al.*, Nucl. Instr. and Meth. **A428** (1999) 403.
- [4] R.Veenhof, Nucl. Instr. and Meth. **A419** (1998) 726;  
<http://consult.cern.ch/writeup/garfield>.
- [5] S.F. Biagi, Nucl. Instr. and Meth. **A283** (1989) 716.
- [6] S.F. Biagi, Nucl. Instr. and Meth. **A421** (1999) 234.
- [7] T.Kleinknecht, Detektren Für Teilchenstrahlung, B.G.Teubner. Stuttgart (1984).
- [8] L.G.H. Huxley and R.W. Crompton, The Diffusion and Drift of Electrons in Gases (Wiley, New York, 1974) Chap.8.
- [9] T.Kunst *et al.*, Nucl. Instr. and Meth. **A324** (1993)127.
- [10] Y. H. Chang *et al.*, Nucl. Instr. and Meth. **A339** (1994) 524.
- [11] J. Va'vra *et al.*, Nucl. Instr. and Meth. **A324** (1993) 113.
- [12] Cube Beam Splitter, SIGMA KOKI Corporation, Japan.
- [13] N. Okazaki, Thesis, Tokyo Univ. of Agriculture and Technology (1999).
- [14] B.CDC AMP DISCRI TYPE II, Electronics division, KEK, Japan.
- [15] FADC RPC-250, REPIC Corporation, Japan.
- [16] R. Robson, M. Hildebrandt, and B. Schmidt, Nucl. Instr. and Meth. **A394** (1997) 74.
- [17] U.J. Becker *et al.*, Nucl. Instr. and Meth. **A360** (1995) 476.
- [18] A. Breskin *et al.*, Nucl. Instr. and Meth. **124** (1975) 189.
- [19] R.D. Hake and A.V. Phelps, Phys. Rev. **158** (1967) 70.
- [20] T. Tauchi, Talk presented at ACFA/LCWS99, Taipei, Taiwan (1999).